

Ultrafast Carrier Dynamics in Colloidal WS₂ Nanosheets obtained through a Hot Injection Synthesis

Pengshang Zhou,¹ Ivo Tanghe,^{1,2} Pieter Schiettecatte,¹ Dries van Thourhout,² Zeger Hens,¹ and Pieter Geiregat^{1,*}

¹*Physics and Chemistry of Nanostructures Group, Department of Chemistry, Ghent University, Krijgslaan 281-S3, 9000 Gent, Belgium*

²*Photonics Research Group, Department of Information Technology, Ghent University, Technologiepark-Zwijnaarde 126, 9052, Gent, Belgium*

(Dated: October 3, 2019)

In recent years, hot injection synthesis has emerged as a promising route for the production of nanostructured transition metal dichalcogenides (TMDs), in large due to its better control over the crystallinity and monodispersity compared to other solution based methods. Understanding the photo-physics of excitons in the thus obtained colloidal nanosheets is of great importance to explore their potential for applications in opto-electronics. Here, we study the carrier dynamics in these few-layer colloidal WS₂ nanosheets by use of broadband transient absorption spectroscopy. The dynamics of both the bleach, linewidth broadening and energy shift across the entire visible and near-infrared spectrum, allows us to identify sub-picosecond electron trapping as the main carrier loss channel. A more quantitative analysis shows that the intrinsic properties of colloidally synthesized nanosheets are on par with other synthesis methods, paving the way for this method to produce high quality nanosheets.

I. INTRODUCTION

Transition metal dichalcogenides (TMDs) have attracted much research interest in recent years due to their interesting optical and electrical properties.[1–6] Often called layered semiconductors, these materials are characterized by strong covalent bonding in-plane and weak van der Waals interactions between the layers. The weak forces between adjacent layers allow them to be isolated as single-layer or few-layer sheets, which show different properties compared to their bulk counterparts, such as a transition from indirect to direct band gap behavior and peculiar valley-selective spin properties.[2, 4, 5, 7, 8] Of the various TMDs, WS₂ in the semiconducting 2H-phase is particularly promising due to its larger spin-orbit interaction,[9–11] offering a robust platform to study spin and valley physics, as well as potential for large material gain and low population inversion thresholds[12], required to produce net stimulated emission[13] and build micro-lasers. [14]

Much of the work to date is concentrated on TMDs obtained by exfoliation, either mechanical or liquid phase assisted,[15–19] or by means of chemical vapor deposition (CVD).[20–24] While the latter has produced high quality sheets with controllable thickness, the need of expensive vacuum deposition and substrate matched growth conditions might eventually limit their mass production. Exfoliation could present a viable alternative to CVD, yet the limited control over sheet thickness, surface area or surface stabilization restricts the application potential. As an alternative method to prepare TMDs, a bottom-up colloidal synthesis offers a unique way to produce TMD nanosheets in large quantities with controllable dimensions and surface properties.[25–28]

In a recent study by Schiettecatte *et al.*,[29] the ultrafast carrier dynamics in colloidally synthesized MoS₂ nanosheets

were studied. The carrier dynamics after photo-excitation observed in that work seemed on-par with state-of-the-art CVD and exfoliated samples. Since WS₂ has similarly intriguing properties as MoS₂,[1] unravelling the basic photo-physics of colloidal WS₂ nanosheets is equally important to advance their further use in optoelectronics.

Here, we report on the carrier dynamics in WS₂ nanosheets obtained through a hot injection synthesis by use of broadband ultrafast transient absorption (TA) spectroscopy. We show that state filling by electrons and holes contributes to the bleach of *A* and *B* exciton features, whereas a strong band gap reduction leads to an overall red-shift of the spectra, as previously reported for TMDs nanosheets. By means of a detailed deconvolution of the complete absorption spectrum, we find a common ultrafast timescale for the *A* and *B*-exciton bleach recovery, indicating fast electron capture by defects. Moreover, we do not observe strong dependence of spectral signatures on pump photon energy, which hints towards limited temperature effects. Given that similar carrier dynamics have been demonstrated in both CVD-grown WS₂ monolayers[23] and liquid phase-exfoliated WS₂ multilayers,[30] we conclude that a bottom-up synthesis can produce nanosheets of comparable quality as more commonly used techniques, yet has the potential to be used in solution-based processes with associated merits of cost-effectiveness and increased compatibility with different substrates.

II. MATERIALS AND TECHNIQUES

A. Chemicals

Tungsten hexacarbonyl (W(CO)₆, 99.99%, Sigma Aldrich), oleic acid (90%, Alfa Aesar), oleylamine (80-90%, Acros Organics), trioctylphosphine oxide (TOPO, reagent plus, 99%), squalane(98%, Alfa Aesar), 1,2-dichlorobenzene (DCB) (99%, Acros Organics). All materials were used as received.

* Pieter.Geiregat@UGent.be.

B. Colloidal Synthesis of WS₂

In a typical synthesis, 0.1 mmol W(CO)₆ was added into the flask with 0.4 mL oleic acid, 2.4 mL oleylamine, 2 g TOPO and 4 mL squalane. The mixture was first degassed at room temperature for 30 min and then at 120 °C for another 30 min under stirring to make sure to get rid of any residual traces of oxygen and water. Meantime, 0.28 mmol S was dissolved into 2 mL of oleylamine to prepare OLA-S precursor. After degassing, the flask was filled with nitrogen and heated up to 330 °C at which point the OLA-S was injected into the flask. The reaction mixture was kept at 330 °C for 1h before it was cooled down. When the temperature went down to 80 °C, 8 mL toluene was added into the flask to prevent TOPO from solidifying. 12 mL of methanol was used to precipitate the nanosheets followed by centrifugation at 4000 rpm. The nanosheets were washed twice more with toluene and methanol and were finally dispersed in DCB for further use.

C. Basic Characterization of WS₂

Bright field transmission electron microscopy (TEM) images were taken on a Cs-corrected JEOL 2200-FS TEM operated at an acceleration voltage of 200 kV. Absorption spectra were recorded on a Perkin Elmer Lambda 950 spectrometer. Atomic force microscopy (AFM) was performed using a Bruker Dimension Edge with a NCHV probe with tapping mode in air. X-ray diffraction (XRD) measurements were carried out on a Thermo Scientific ARM X'tra X-ray diffractometer with the Cu K α line as primary source. For Raman analysis, a KAISER dispersive RXNI spectrometer was used operating at 532 nm with a 1 cm⁻¹ spectral resolution.

D. Transient Absorption Spectroscopy

Transient absorption spectra were obtained by exciting colloidal dispersions of WS₂ in DCB using 110 femtosecond pump pulses with varying wavelengths (400 nm, 600 nm) obtained from the 800 nm output of a 1 kHz Ti:S laser system through non-linear conversion in an OPA. Probe pulses in the visible and near infrared window were generated by passing the 800 nm fundamental through a thin sapphire or YAG crystal, respectively. The pulses were delayed relative to the pump using a delay stage up to 3 ns. The probe spectrum in our experiments was collected using a 0.22 NA 200 micron optical fiber (Thorlabs) and detected using silicon or InGaAs line array cameras. The sheets were dispersed in DCB and continuously stirred to avoid photo-charging or degradation. Photon fluxes were determined using a Thorlabs CCD camera beam profiler and a thermal power sensor.

III. RESULTS AND DISCUSSION

A. Linear properties of WS₂ nanosheets

WS₂ nanosheets were prepared by a hot-injection synthesis producing colloidally dispersed sheets, see the Materials section for more details. Figure 1a shows a typical high-resolution TEM image of the obtained sample, which indicates the few-layer nanosheets are in the desired semiconducting 2H phase. X-ray powder diffraction (XRD, Supporting Information S-I) was used to demonstrate the sample is indeed 2H WS₂. The broadened (002) peak indicates the synthesized nanocrystals have a small lateral size, typically below \approx 100 nm as shown in Supporting Information Figure S-I. Compared with the nanosheets obtained from liquid-exfoliated method, the nanosheets here have higher aspect ratio.[32] Atomic force microscopy (AFM) was used to determine the average thickness at 1.30 ± 0.05 nm, see Figure 1b. Such a thickness corresponds to 2 or 3 layers of WS₂. [33] High-resolution TEM images also highlight the few-layer structure, see Supporting Information Figure S-II. We further cross-check the phase and thickness of the nanosheets using Raman spectroscopy, see Figure 1c. The shifts of the vibrational modes, as well as the decreased frequency difference between these two modes, compared with the bulk WS₂, also indicate the formation of few-layered WS₂ in the 2H-phase.[34, 35] The absorption spectrum of the sample in Figure 1d exhibits distinct peaks at 612 nm (2.02 eV), 518 nm (2.39 eV) and 440 nm (2.82 eV) labeled as A, B and C, respectively. As stated in several literature reports, A and B originate from the excitonic transitions at the K point of the Brillouin zone, coupling two distinct spin-orbit split valence bands to the same conduction band level. The local maximum C corresponds to transitions between the parallel density of states along $\Gamma - K$ in the valence and conduction bands.[31]

B. Carrier recombination in two stages

To study the carrier dynamics in our colloidal WS₂ nanosheets, we use femtosecond transient absorption spectroscopy, a technique that measures the change in absorption ΔA over a broad wavelength range after photo-excitation with an off- or on-resonance pump pulse, here at 400 nm and 600 nm, respectively. Figure 2a and 2b show the 2D map of $\Delta A(\lambda, t)$ for 400 nm (a, left column) and 600 nm (b, right column) excitation. To obtain a first global insight into the carrier dynamics and spectral response, we focus on the kinetics at fixed wavelengths (Figure 2c, 2d) or the spectra at fixed delay (Figure 2e, 2f). For the former, we plot the kinetics at the A exciton position (612 nm) and monitor its pump power dependence, both for 400 nm (Figure 2c) and 600 nm (Figure 2d) excitation. The pump power is expressed as a sheet density n_s , in cm⁻², see also Supporting Information S-II, ranging from 8.9×10^{11} to 2.7×10^{13} cm⁻². We note that the Mott density, a density where the exciton gas transitions into a plasma state, is estimated at 10^{13} cm⁻². [23, 36] As shown in the insets of Figure 2c and 2d, we observe two distinct rates,

This is the author's peer reviewed, accepted manuscript. However, the online version of record will be different from this version once it has been copyedited and typeset.
PLEASE CITE THIS ARTICLE AS DOI:10.1063/1.5124898

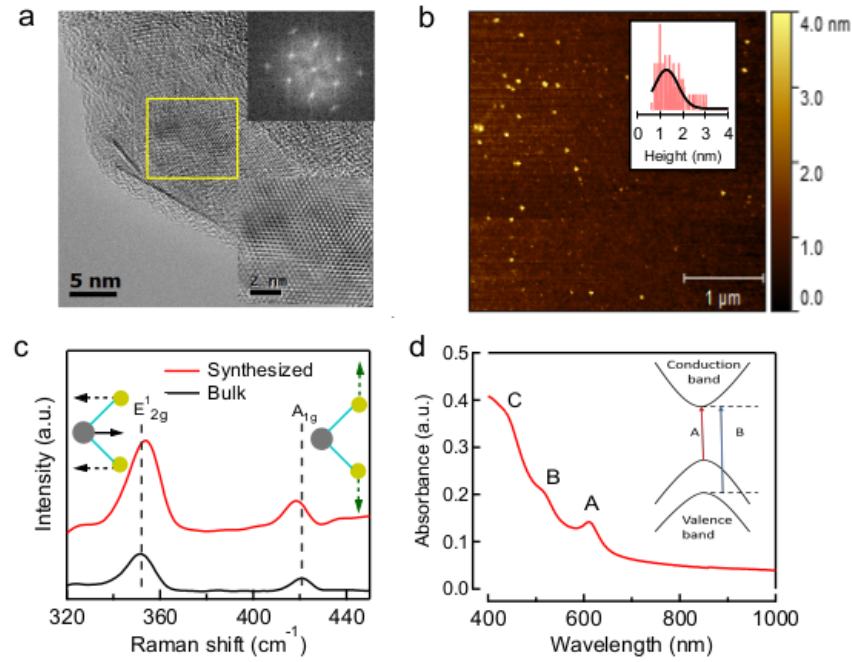


FIG. 1. Characterization of the colloidal WS_2 nanosheets used in this study. (a) High-resolution TEM image of the nanosheets. Insert in (a): The FFT pattern (top right) and filtered HRTEM image (right bottom) of the area enclosed by the yellow square. (b) AFM image of WS_2 nanosheets spincoated on a silicon substrate, where the inset shows the height histogram based on 100 nanosheets. (c) Raman spectra of the colloidal nanosheets (red) and bulk WS_2 (black). The vertical dashed lines indicate the positions of the bulk vibrations E_{2g} and A_{1g} . (d) UV-vis absorption of the nanosheets dispersed in dichlorobenzene (DCB) with A, B and C exciton transitions indicated. Inset shows a schematic of the single particle levels involved in the A and B excitonic transitions.[31]

indicative of two different regimes of carrier recombination. A first regime is characterized by rates of 1.52 (400 nm) to 2.64 ps^{-1} (600 nm), the second stage is characterized by rates of 0.04 ps^{-1} (400 nm) and 0.097 ps^{-1} (600 nm). The slow decays here are in line with the values that have been reported by Vega-Mayoral *et al.* for exfoliated sheets.[37] The small difference under the two excitation conditions can most likely be ascribed to a timescale required for charge cooling in the case of 400 nm excitation, in particular for the ultrafast stage 1. Importantly, the rates are independent of sheet density for both regimes. We refer to Supporting Information S-III for an overview on the kinetics at the position of A exciton under the various sheet densities.

Observing the 2D maps in Figures 2a and 2b, one notices that in the second stage of recombination, after *ca.* 2 ps, the TA spectrum hardly changes its shape and is characterized by an alteration of positive and negative lobes decaying uniformly. This shape resembles the derivative of the absorption spectrum, as is demonstrated in Figure 2e and 2f where the ΔA spectrum at 10 ps (black trace) is shown together with the first derivative on an energy scale. The excellent correspondence indicates that at late times the shape of the spectrum originates predominantly from a spectral shift. Indeed, in the limit of small energy shifts, Geiregat *et al.* showed that $\Delta A = \Delta E \times \frac{dA_0}{dE}$ [38], where A_0 is the linear absorption spectrum and ΔE is the energy shift of the linear spectrum. From the traces in Figure 2e and 2f, we can deduce a redshift of 1.6

meV for the 400 nm pump ($8.9 \times 10^{12} \text{ cm}^{-2}$) and a comparable 1.4 meV in case of 600 nm pump ($5.08 \times 10^{12} \text{ cm}^{-2}$). Deviations between the spectral shift prediction and the experimental traces mainly occur at the A and B -exciton position, most likely due to the residual bleach associated with state filling, see further. We conclude that the transient absorbance is dominated by spectral shifts at time delays beyond 10 ps, an observation in line with numerous reports on CVD and exfoliated TMDs systems.[18, 23, 39]

C. Detailed analysis

Transient absorption spectra present a complex interplay between spectral shifts, broadening and bleach (reduced absorption) of the exciton transitions. Both the shifts and broadening are affected by carrier temperature and density, whereas the bleach is typically directly correlated to carrier density. Clearly, extracting the bleach is key to evaluate carrier dynamics and the single wavelength and/or time slices of Figure 2 only present a first indication of these carrier dynamics. In order to develop a complete picture of both the fast stage 1 and the shift-dominated stage 2, we perform a fitting procedure to extract the effects of photo-excitation on the exciton area S , exciton peak position $E_{A,B}$ and linewidth Γ . The latter two can be affected by the carrier density and temperature, whereas the exciton area reduction is related directly to state filling.

This is the author's peer reviewed, accepted manuscript. However, the online version of record will be different from this version once it has been copyedited and typeset.
PLEASE CITE THIS ARTICLE AS DOI:10.1063/1.5124898

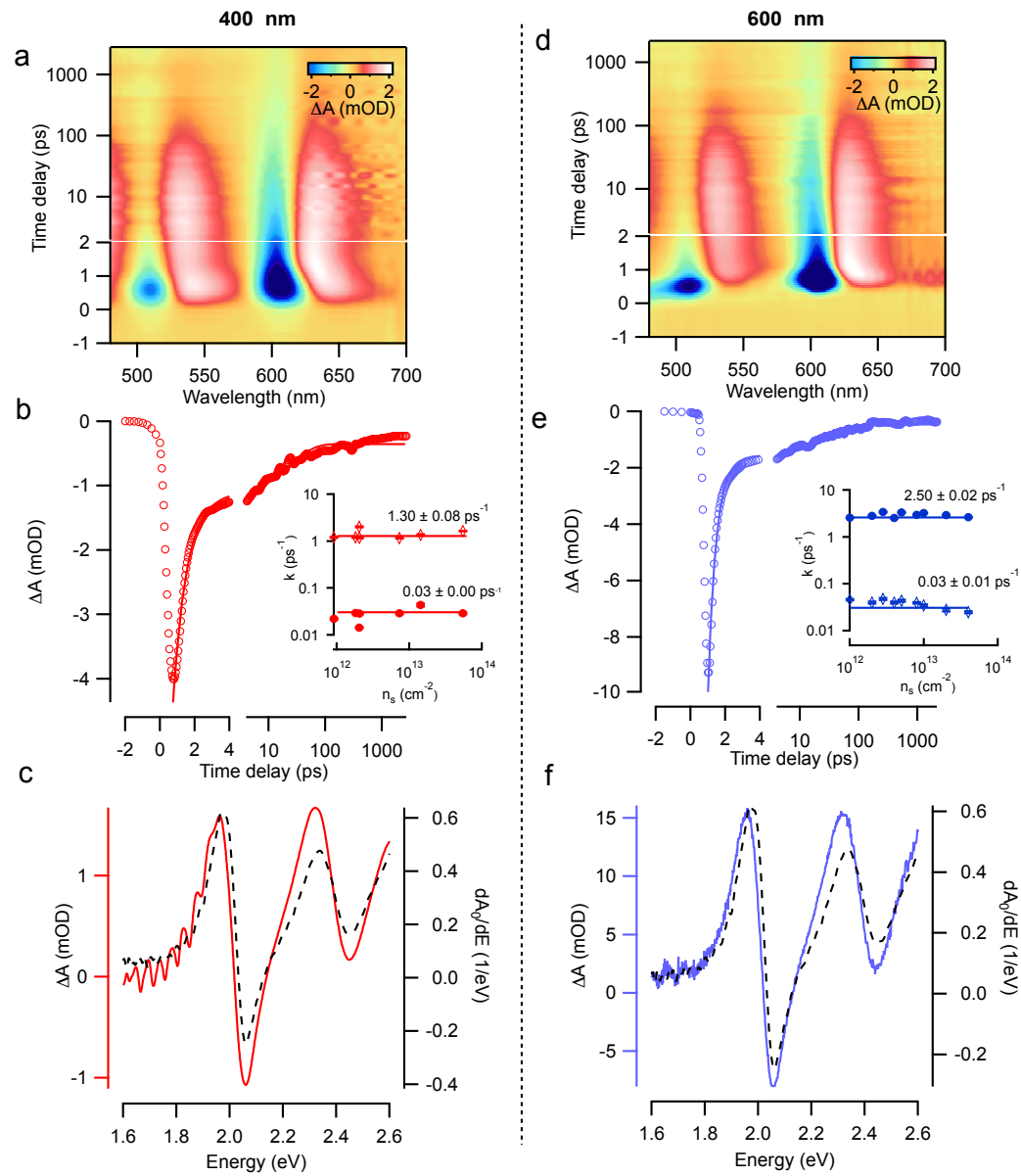


FIG. 2. Transient absorption spectroscopy. (a,b) False color map of ΔA upon photo-excitation at (a) 400 nm for a sheet density of $8.79 \times 10^{12} \text{ cm}^{-2}$ and (b) 600 nm for a sheet density of $5.08 \times 10^{12} \text{ cm}^{-2}$. (c,d) ΔA at the position of the A-exciton (612 nm) for 400 nm (c) and 600 nm (d) excitation. Insets show the decay rates vs the sheet density, as obtained from bi-exponential fits to the respective kinetic traces. (e,f) Comparison the derivative $\frac{dA_0}{dE}$ of the linear absorption (black, dashed) with the transient absorption ΔA spectrum at 10 ps time delay. The sheet densities here are the same as that used in a and b, respectively.

Supporting Information S-IV describes the fitting procedure in more detail. In short, we model the absorption spectrum on an energy scale as a sum of two gaussian functions imposed on a polynomial background. First, a fit is developed for the linear absorption spectrum A_0 , resulting in parameters E_0 , S_0 and Γ_0 , for both the A and B exciton line. Next, we sum the transient absorbance ΔA together with A_0 to obtain the absorbance at a given time delay, $A(E, t) = \Delta A(E, t) + A_0(E)$. Fitting the latter produces at every time delay the peak position $E(t)$, area $S(t)$ and linewidth $\Gamma(t)$, again for A and B. Finally, we calculate the change of these parameters: $\Delta E(t) = E(t) - E_0$,

$\Delta S(t) = S(t) - S_0$ and $\Delta \Gamma(t) = \Gamma(t) - \Gamma_0$. As we observed in Figure 2e and 2f, the spectrum is dominated by a uniform shift at later time delays. We implement this in the procedure by using a fixed shift ΔE across the spectrum, *i.e.* for both A, B and the background.

Figure 3a-c shows the results of this procedure for an experiment with 400 nm pump, creating an initial sheet density of $8.79 \times 10^{12} \text{ cm}^{-2}$. Similar to Figure 2c, we observe two distinct stages of recombination. First, a rapid drop of the exciton area S occurs due to state filling (Figure 3a), which is accompanied by line-width broadening (Figure 3b) and a red-

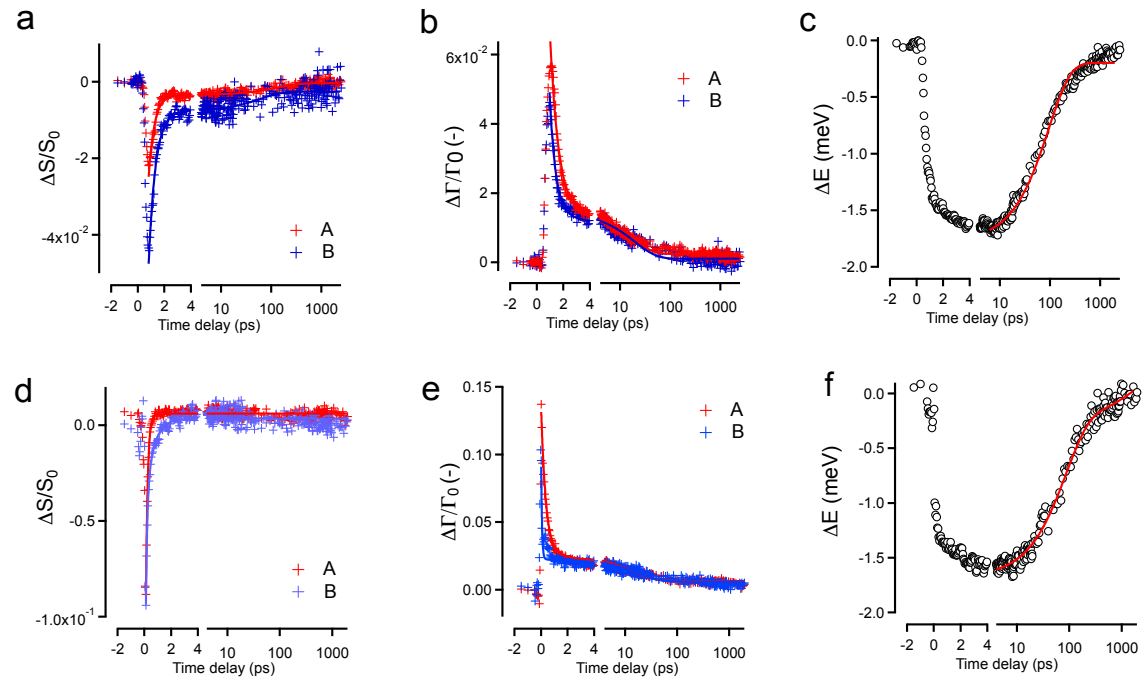


FIG. 3. (a-c) Relative area change $\Delta S/S_0$, relative linewidth change $\Delta\Gamma/\Gamma_0$ and the shift of peak energy ΔE for (a-c) 400 nm pump with a sheet density of $8.79 \times 10^{12} \text{ cm}^{-2}$ and (d-f) 600 nm pump with a sheet density of $5.08 \times 10^{12} \text{ cm}^{-2}$.

shift ($\Delta E < 0$, Figure 3c) rising to 1.6 meV in 0.48 ps, *i.e.* a rate of 1.9 ps^{-1} . Next, The A and B area bleach recover at a rate of 2.26 ps^{-1} and 1.91 ps^{-1} , respectively. The recovery of the linewidth in the first stage proceeds with a rate of 1.79 ps^{-1} and 2.21 ps^{-1} , in large similar to the bleach recovery. This overall recovery at a *ca.* 2 ps^{-1} rate is in good agreement with the rates obtained from the qualitative fit in Figure 2c. Importantly, this ultrafast bleach recovery is unambiguously imprinted on both the A and B exciton resonance. Figure 3c shows that the redshift ($\Delta E < 0$) stays nearly constant during the first 10 ps.

At longer time delays, beyond *ca.* 2 ps, a second stage starts where the area bleach and linewidth of A and B recover at much slower rates indicated by the rate constants of 0.01 and 0.02 ps^{-1} for the area recovery and 0.07 and 0.05 ps^{-1} for the linewidth. Also here, the slow recombination is in line with the qualitative observations of Figure 2 where we observed a second slow regime of carrier recombination. The spectral shift recovers somewhat faster at a rate of 0.01 ps^{-1} , yet in large also comparable to the second stage of the area bleach and line-width recovery.

It is well known that the observed shifts and broadening of the exciton resonances can also originate from temperature effects, see further, where reports have shown that increased lattice temperatures give rise to exciton redshifts and/or broadening.[13, 18] To study this in more detail, we also analyzed the resonant pump experiments using the same fitting algorithm, as in this scenario no excess energy relative to the band edges is deposited in the nanosheets. Figure 3d-f show the results in a similar fashion as for the 400 nm exci-

tation, where we again observe two regimes. A first rapid recovery of the A and B area bleach and linewidth is followed by a slower second stage which is less pronounced than that for 400 nm. For the first stage, the fitting of the area recovery on A excitation results in a rate constant of 7.1 ps^{-1} , which is close to the time resolution of the experiment at 8 ps^{-1} , while the B recovers at a resolution limited rate (listed as IRF in Table 1) and slower rate of 1.68 ps^{-1} , which are much faster compared with the ones at 400 nm pump. The trapping rates are much higher compared to exfoliated WS₂ multilayers, which suggests a much higher trap content exist in this nanosheets.[30]

The spectral shift recovers at a different pace in the first stage, remaining constant in the first 10 ps, only to recombine again with a 0.01 ps^{-1} rate in a second stage. Moreover, the shift is comparable in magnitude to the shift for the 400 nm experiment in Figure 3c. For clarity, Table I summarizes the different rates for both 400 and 600 nm excitation.

Even though the fit model clearly indicates a rapid initial loss of charge carriers through the strong loss of the exciton area bleach of both exciton features, we cross-check the carrier dynamics using a probe that is insensitive to broadening or shifts. In particular, by probing in the near-infrared we address intraband transitions which are spectrally flat, yet probe the sum of electron and hole density simultaneously.[15, 29] Figure 4a shows the result of such an experiment for a 400 nm pump where we probe the transient absorption change at 1100 nm and fit its kinetics using a double-exponential function. Again, the decay can be fitted with a fast stage of 0.80 ps^{-1} and a slower rate of 0.021 ps^{-1} , in line with the two decay stages and rates we observed in Figures 2 and 3.

TABLE I. Fitting results for the rates under 400 nm and 600 nm excitation.

	400 nm		600 nm	
	Stage I (ps ⁻¹)	Stage II (ps ⁻¹)	Stage I (ps ⁻¹)	Stage II (ps ⁻¹)
$\Delta S_A/S_{0,A}$	2.26 ± 0.08	0.01 ± 0.001	7.10 ± 0.20	-
$\Delta S_B/S_{0,B}$	1.91 ± 0.09	0.02 ± 0.003	<i>IRF</i>	1.68 ± 0.21
$\Delta \Gamma_A/\Gamma_{0,A}$	1.79 ± 0.05	0.07 ± 0.003	2.78 ± 0.05	0.07 ± 0.003
$\Delta \Gamma_B/\Gamma_{0,B}$	2.21 ± 0.10	0.05 ± 0.003	<i>IRF</i>	0.06 ± 0.005
ΔE	-	0.01 ± 0.0002	-	0.01 ± 0.0003

D. Model for carrier recombination in WS₂ nanosheets

The similar ultrafast bleach recovery of the *A* and *B* excitation area indicate a common loss channel for both transitions. Since only the electron level is common to both transitions, see inset Figure 1d, we attribute the first stage of carrier recombination to a fast loss of the electron population. The fluence independent nature of the recombination channel indicates it is linked to charge carrier trapping, since both geminate two and three-body recombination would require a density dependent scaling of the recombination time.[17, 40, 41] The strong carrier trapping in our colloidal sheets impedes any comparison to exciton-exciton annihilation directly.[42] For colloidal MoS₂ obtained via a similar hot injection synthesis, Schiettecatte *et al.*[29] reported an asymmetry between the *A* and *B* exciton bleach recovery, indicating a prevalent hole-trapping mechanism. We should note that this does not necessarily indicate a different trap since the activity of deep defects can depend on the position of the Fermi level.[43–45]

The fluence independent and slower second stage of recombination could be assigned to recombination of trapped electrons with the remaining holes, see the schematic in Figure 4b. Wang and coworkers observed a qualitatively similar two-step fluence-independent recombination process, which they assigned to electron-assisted Auger trapping.[15] We cannot make this statement here quantitatively due to our limited knowhow of the background doping of the colloidal sheets used.

E. Discussion of the exciton energy shift

The energy shifts ΔE shown in Figures 3c and 3f displays quite remarkable behavior as they are nearly similar for resonant (600 nm) and non-resonant excitation (400 nm) at fixed sheet density, see Figure 4c (top), they build up instantly in both cases but stay nearly constant during the first stage of rapid electron trapping. The slow decay of the energy shift at 0.01ps^{-1} does line up with the second stage of hole recombination, likely indicating that the shift is connected to the carrier density. Figure 4c shows the increase of the energy shift with increasing sheet density for both 400 (blue markers) and 600 nm (red markers) excitation, reaching a maximum value of 6.7 meV at $n_s = 2.6 \times 10^{13} \text{ cm}^{-2}$.

The energy shift ΔE of an exciton line originates from an interplay between binding energy reduction (BER), causing blueshifts or energy increase, and band gap renormalization

(BGR), causing redshifts. We note that the energy shifts are too small to originate from trions.[46, 47]

Both an increased sheet density and lattice temperature can cause BER and BGR. The rapid loss of band edge carriers will disable the contribution of geminate exciton-exciton annihilation to heating. Nonetheless, non-radiative recombination through defect states typically also proceeds via phonon emission and could hence also heat up the system. Focusing first on temperature, Supporting information S-VI shows that an increased lattice temperature should lead to a redshift, as observed in exfoliated and CVD grown-TMD systems.[24, 48, 49] However, no difference is observed between resonant and non-resonant excitation even though in the case of non-resonant excitation up to 1 eV, *i.e.* roughly 500 meV per carrier, of excess energy is dissipated into the sheets.[49] We can conclude that carrier temperature plays only a minor role in the observed energy shift opposed to some literature reports.[18] Leaving out temperature, we assign the shift to carrier density induced effects. As the shift is a net redshift, we hence conclude that BGR is the dominant effect, in-line with similar reports on nanosheets produced from CVD methods.[16] In their work on MoS₂ sheets, Sie *et al.* proposed a model for the carrier density dependence of the energy shift[47]:

$$\frac{\Delta E}{E_{b,X}} = -\gamma(n_s \pi a_B^2)^k \quad (1)$$

where γ is a constant that is specific for the exciton type, $E_{b,X}$ is the exciton binding energy and a_B is the Bohr radius. For WS₂, we can estimate $E_{b,X} \approx 300 \text{ meV}$ [50] and $a_B \approx 1 \text{ nm}$. The coefficient k depends on the type of Coulomb interactions that dictate the correlations and the ensuing energy shifts. For $k = 1$ long range interactions dominate, whereas short range interactions imply a $k = 1/2$ law. The data obtained here can be fitted using $k = 2/3$, see Figure 4c (bottom), a value intermediate to both regimes and in line with reports on MoS₂, see Figure 4c (bottom).[47]

We can compare our obtained shift values to the report of Ruppert *et al.*[18] where values of 10 meV were found for CVD grown single layer WS₂ at a pump fluence of $100 \mu\text{J}/\text{cm}^2$, which in our experiment would produce a shift of only 1.6 meV, see Supporting Information S-II, nearly one order of magnitude smaller. We can rationalize this by considering that the energy shifts depend strongly on carrier density, which in our colloidal sheets suffers a substantial loss due to fast electron trapping. Indeed, Figure 3 suggests a drop in car-

rier density of close to 90 %, in line with the nearly one order of magnitude reduced shift compared to literature.

IV. CONCLUSIONS

Multi-layered WS₂ nanosheets obtained through a direct colloidal synthesis were studied using femtosecond transient absorption spectroscopy. The carrier dynamics indicate fast electron trapping, followed by slower Auger-assisted hole recombination. The spectra at late times are dominated by spectral shifts originating from a strong carrier density induced band gap renormalization. Given that similar carrier dynamics and photophysics have been demonstrated in CVD-grown WS₂ nanosheets, we can conclude that colloidal synthesis can produce multi-layered WS₂ nanosheets of a quality in line with CVD methods. The colloidal sheets seem to be subject to the same defects and could hence benefit from established optimization procedures. Together with their cost-effective solution based fabrication and processing, colloiddally synthesized

WS₂ nanosheets could take a firm foothold in both the colloidal quantum dot and TMD communities.

V. SUPPLEMENTARY MATERIAL

The Supplementary Material contains information on the samples (synthesis, structural characterization), the transient absorption spectroscopy and the fitting procedure.

ACKNOWLEDGMENTS

Z.H. acknowledges support by the European Commission via the Marie-Sklodowska Curie action Phonsi (H2020-MSCA-ITN-642656), the Research Foundation Flanders (project 17006602) and Ghent University (GOA no. 01G01513). P.Z. thanks the China Scholarship Council (CSC) and Ghent University BOF-cofunding for the financial support. P.S. acknowledges FWO-Vlaanderen for a fellowship (FWO-SB scholarship).

-
- [1] Q. H. Wang, K. Kalantar-Zadeh, A. Kis, J. N. Coleman, and M. S. Strano, *Nature nanotechnology* **7**, 699 (2012).
- [2] D. Ovchinnikov, A. Allain, Y.-S. Huang, D. Dumcenco, and A. Kis, *ACS nano* **8**, 8174 (2014).
- [3] P. Zhou, Q. Xu, H. Li, Y. Wang, B. Yan, Y. Zhou, J. Chen, J. Zhang, and K. Wang, *Angewandte Chemie International Edition* **54**, 15226 (2015).
- [4] H. Tan, Y. Fan, Y. Zhou, Q. Chen, W. Xu, and J. H. Warner, *ACS nano* **10**, 7866 (2016).
- [5] Y. Yue, J. Chen, Y. Zhang, S. Ding, F. Zhao, Y. Wang, D. Zhang, R. Li, H. Dong, W. Hu, *et al.*, *ACS applied materials & interfaces* **10**, 22435 (2018).
- [6] M. Chhowalla, H. S. Shin, G. Eda, L.-J. Li, K. P. Loh, and H. Zhang, *Nature chemistry* **5**, 263 (2013).
- [7] K. F. Mak, C. Lee, J. Hone, J. Shan, and T. F. Heinz, *Physical review letters* **105**, 136805 (2010).
- [8] F. Raza, J. H. Park, H.-R. Lee, H.-I. Kim, S.-J. Jeon, and J.-H. Kim, *ACS Catalysis* **6**, 2754 (2016).
- [9] R. Coehoorn, C. Haas, and R. De Groot, *Physical Review B* **35**, 6203 (1987).
- [10] Y. Ding, Y. Wang, J. Ni, L. Shi, S. Shi, and W. Tang, *Physica B: Condensed Matter* **406**, 2254 (2011).
- [11] Z. Zhu, Y. Cheng, and U. Schwingenschlögl, *Physical Review B* **84**, 153402 (2011).
- [12] F. Lohof, M. Florian, M. Lorke, D. Erben, F. Jahnke, and C. Gies, *Nano Letters* (2019), 10.1021/acs.nanolett.8b03729.
- [13] A. Chernikov, C. Ruppert, H. M. Hill, A. F. Rigosi, and T. F. Heinz, *Nature Photonics* **9** (2015), 10.1038/nphoton.2015.104.
- [14] Y. Ye, Z. J. Wong, X. Lu, X. Ni, H. Zhu, X. Chen, Y. Wang, and X. Zhang, *Nature Photonics* **9**, 733 (2015).
- [15] H. Wang, C. Zhang, and F. Rana, *Nano letters* **15**, 339 (2014).
- [16] E. A. Pogna, M. Marsili, D. De Fazio, S. Dal Conte, C. Manzoni, D. Sangalli, D. Yoon, A. Lombardo, A. C. Ferrari, A. Marini, *et al.*, *ACS nano* **10**, 1182 (2016).
- [17] G. Kime, M. A. Leontiadou, J. R. Brent, N. Savjani, P. O'Brien, and D. Binks, *The Journal of Physical Chemistry C* **121**, 22415 (2017).
- [18] C. Ruppert, A. Chernikov, H. M. Hill, A. F. Rigosi, and T. F. Heinz, *Nano letters* **17**, 644 (2017).
- [19] D. Tsokkou, X. Yu, K. Sivula, and N. Banerji, *The Journal of Physical Chemistry C* **120**, 23286 (2016).
- [20] S. Sim, J. Park, J.-G. Song, C. In, Y.-S. Lee, H. Kim, and H. Choi, *Physical Review B* **88**, 075434 (2013).
- [21] S. H. Aleithan, M. Y. Livshits, S. Khadka, J. J. Rack, M. E. Kordes, and E. Stinaff, *Physical Review B* **94**, 035445 (2016).
- [22] P. D. Cunningham, K. M. McCreary, A. T. Hanbicki, M. Currie, B. T. Jonker, and L. M. Hayden, *The Journal of Physical Chemistry C* **120**, 5819 (2016).
- [23] P. D. Cunningham, A. T. Hanbicki, K. M. McCreary, and B. T. Jonker, *ACS nano* **11**, 12601 (2017).
- [24] T. Jiang, R. Chen, X. Zheng, Z. Xu, and Y. Tang, *Optics express* **26**, 859 (2018).
- [25] B. Mahler, V. Hoepfner, K. Liao, and G. A. Ozin, *Journal of the American Chemical Society* **136**, 14121 (2014).
- [26] H. Lin, C. Wang, J. Wu, Z. Xu, Y. Huang, and C. Zhang, *New Journal of Chemistry* **39**, 8492 (2015).
- [27] D. Son, S. I. Chae, M. Kim, M. K. Choi, J. Yang, K. Park, V. S. Kale, J. H. Koo, C. Choi, M. Lee, *et al.*, *Advanced Materials* **28**, 9326 (2016).
- [28] B.-Q. Zhang, J.-S. Chen, H.-L. Niu, C.-J. Mao, and J.-M. Song, *Nanoscale* **10**, 20266 (2018).
- [29] P. Schiettecatte, P. Geiregat, and Z. Hens, *The Journal of Physical Chemistry C* (2019).
- [30] A. Eva, S. Conte, *et al.*, *Nanoscale* **8**, 5428 (2016).
- [31] G. Pagona, C. Bittencourt, R. Arenal, and N. Tagmatarchis, *Chemical Communications* **51**, 12950 (2015).
- [32] C. Backes, B. M. Szydłowska, A. Harvey, S. Yuan, V. Vega-Mayoral, B. R. Davies, P.-I. Zhao, D. Hanlon, E. J. Santos, M. I. Katsnelson, *et al.*, *ACS nano* **10**, 1589 (2016).
- [33] A. L. Elías, N. Perea-López, A. Castro-Beltrán, A. Berkdemir, R. Lv, S. Feng, A. D. Long, T. Hayashi, Y. A. Kim, M. Endo, *et al.*, *ACS nano* **7**, 5235 (2013).

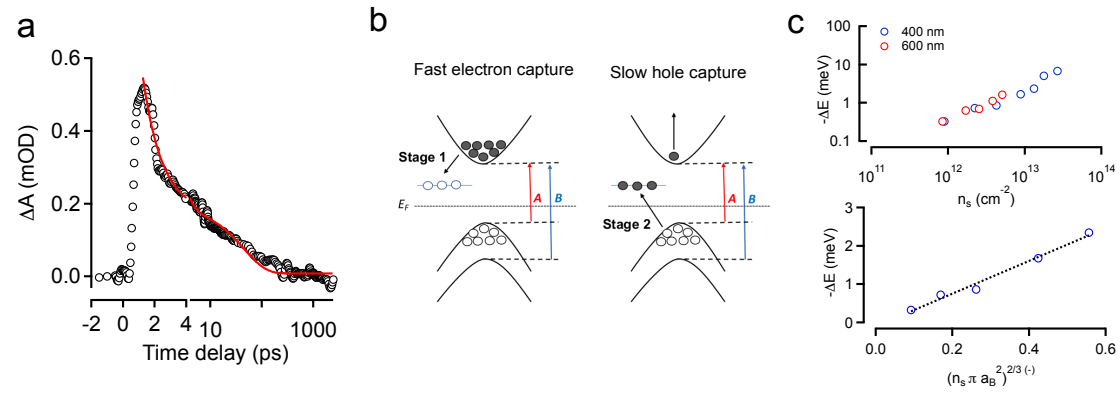
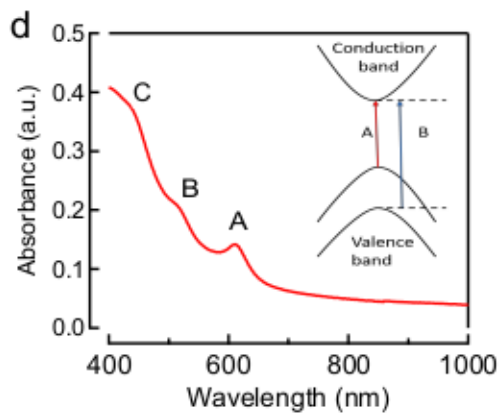
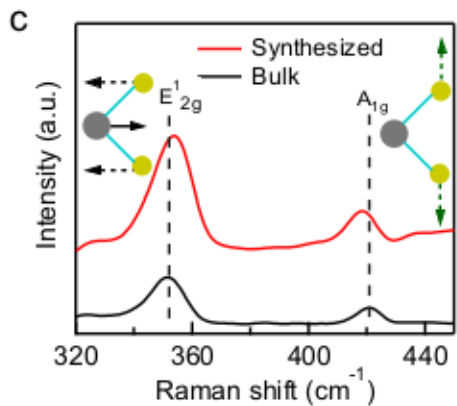
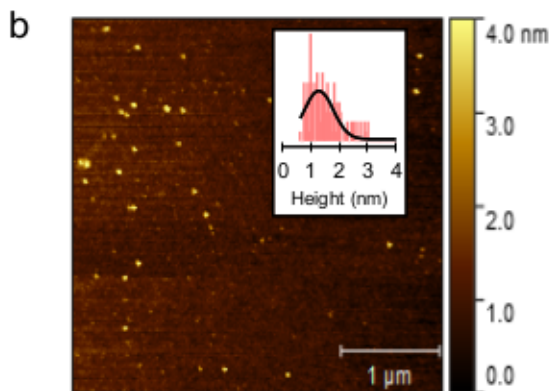
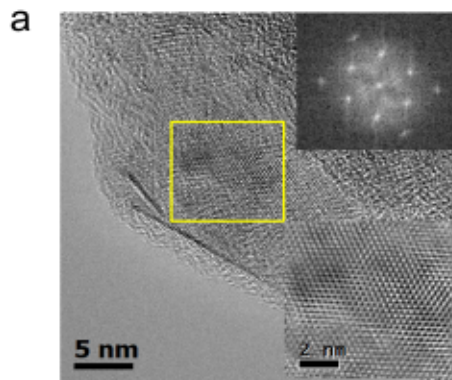
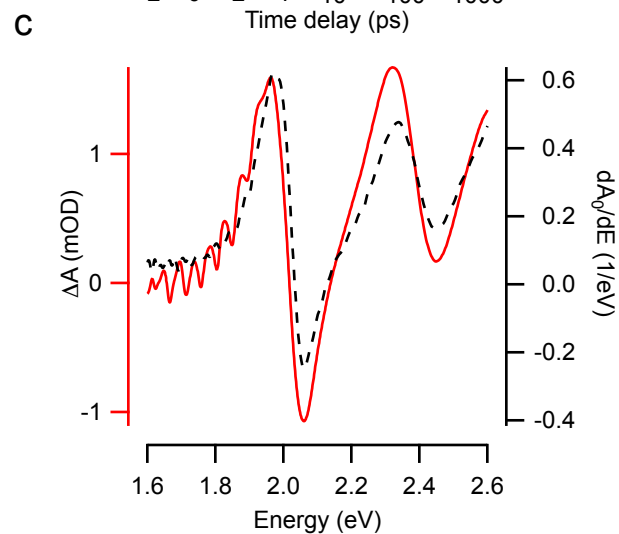
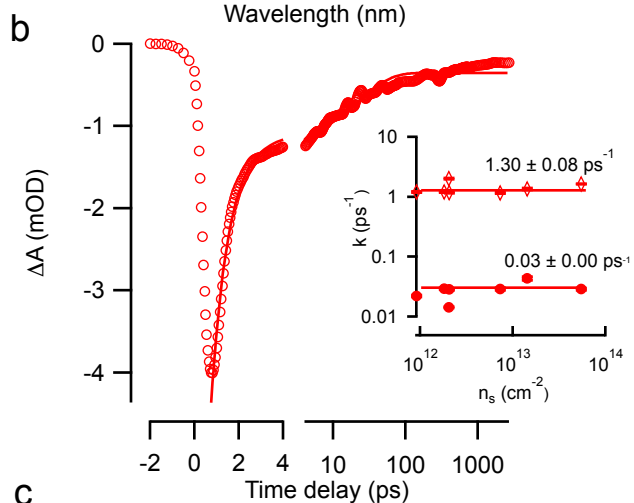
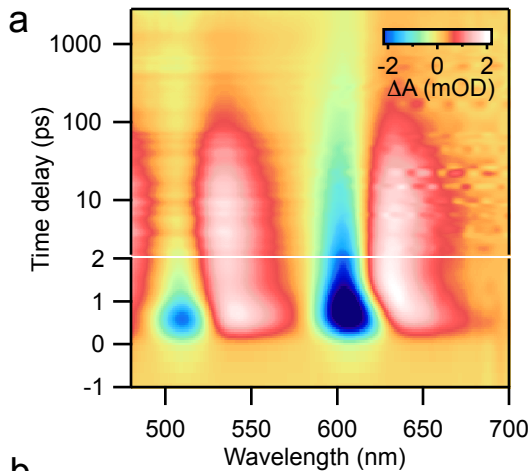


FIG. 4. Carrier recombination models and energy shifts. (a) ΔA at 1100 nm upon excitation at 400 nm with a sheet density of $1.48 \times 10^{13} \text{ cm}^{-2}$. Solid lines indicate a bi-exponential fit to the decay. (b) Schematic of the two-stage carrier capture process upon photo-excitation. First, nearly instant electron trapping reduces the electron population. In a second stage, the residual holes recombine via an Auger-assisted process with the trapped electrons. (c) (top) The energy shift at 3 ps for different sheet densities upon photo-excitation under 400 (blue markers) and 600 nm pump (red markers). (bottom) The energy shift for 400 nm excitation (empty blue markers) versus $(n_s \pi a_B^2)^{2/3}$ together with a linear fit (dashed black line).

- [34] W. Zhao, Z. Ghorannevis, K. K. Amara, J. R. Pang, M. Toh, X. Zhang, C. Kloc, P. H. Tan, and G. Eda, *Nanoscale* **5**, 9677 (2013).
- [35] A. Berkdemir, H. R. Gutiérrez, A. R. Botello-Méndez, N. Perea-López, A. L. Elías, C.-I. Chia, B. Wang, V. H. Crespi, F. López-Urías, J.-C. Charlier, *et al.*, *Scientific reports* **3**, 1755 (2013).
- [36] A. Steinhoff, M. Florian, M. Rösner, G. Schönhoff, T. Wehling, and F. Jahnke, *Nature communications* **8**, 1166 (2017).
- [37] V. Vega-Mayoral, T. Borzda, D. Vella, M. Prijatelj, E. A. Pogna, C. Backes, J. N. Coleman, G. Cerullo, D. Mihailovic, and C. Gadermaier, *2D Materials* **5**, 015011 (2017).
- [38] P. Geiregat, A. Houtepen, Y. Justo, F. C. Grozema, D. Van Thourhout, and Z. Hens, *The Journal of Physical Chemistry C* **118**, 22284 (2014).
- [39] E. J. Sie, A. Steinhoff, C. Gies, C. H. Lui, Q. Ma, M. Rosner, G. Schonhoff, F. Jahnke, T. O. Wehling, Y.-H. Lee, *et al.*, *Nano letters* **17**, 4210 (2017).
- [40] D. Sun, Y. Rao, G. A. Reider, G. Chen, Y. You, L. Brezin, A. R. Harutyunyan, and T. F. Heinz, *Nano letters* **14**, 5625 (2014).
- [41] P. D. Cunningham, K. M. McCreary, and B. T. Jonker, *The journal of physical chemistry letters* **7**, 5242 (2016).
- [42] Y. Yu, Y. Yu, C. Xu, A. Barrette, K. Gundogdu, and L. Cao, *Physical Review B* **93**, 201111 (2016).
- [43] W. van der Stam, M. de Graaf, S. Gudjonsdottir, J. J. Geuchies, J. J. Dijkema, N. Kirkwood, W. H. Evers, A. Longo, and A. J. Houtepen, *ACS nano* **12**, 11244 (2018).
- [44] V. Pinchetti, M. Lorenzon, H. McDaniel, R. Lorenzi, F. Meinardi, V. I. Klimov, and S. Brovelli, *Nano letters* **17**, 4508 (2017).
- [45] S. C. Boehme, T. A. Walvis, I. Infante, F. C. Grozema, D. Vanmaekelbergh, L. D. Siebbeles, and A. J. Houtepen, *ACS nano* **8**, 7067 (2014).
- [46] N. Peimyoo, W. Yang, J. Shang, X. Shen, Y. Wang, and T. Yu, *ACS Nano* **8**, 11320 (2014).
- [47] E. J. Sie, A. J. Frenzel, Y.-h. Lee, J. Kong, and N. Gedik, *Physical Review A* **125**, 011701 (2015).
- [48] W. Zhao, R. M. Ribeiro, M. Toh, A. Carvalho, C. Kloc, A. Castro Neto, and G. Eda, *Nano letters* **13**, 5627 (2013).
- [49] Z. Chi, H. Chen, Z. Chen, Q. Zhao, H. Chen, and Y.-X. Weng, *ACS nano* **12**, 8961 (2018).
- [50] A. Chernikov, T. C. Berkelbach, H. M. Hill, A. Rigosi, Y. Li, O. B. Aslan, D. R. Reichman, M. S. Hybertsen, and T. F. Heinz, *Physical review letters* **113**, 076802 (2014).



400 nm



600 nm

